Switched Self-Sensing Actuator for a MEMS Nanopositioner

Steven Ian Moore
The University of Newcastle
Callaghan, NSW 2308, Australia
E-mail: steven.i.moore@uon.edu.au

Yuen Kuan Yong
The University of Newcastle
Callaghan, NSW 2308, Australia
E-mail: yuenkuan.yong@newcastle.edu.au

S. O. Reza Moheimani
The University of Texas at Dallas
Richardson, TX 75080, USA
E-mail: reza.moheimani@utdallas.edu.

Abstract—This work outlines the instrumentation and actuation of a MEMS nanopositioner, implementing a switching electronics based self-sensing actuation technique. Self-sensing actuation allows for optimal use of transducer die space in MEMS designs. The switching design accommodates actuation voltages of 50 V and is compatible with the silicon-on-insulator microfabrication process. The switching electronics are designed to be directly interfaced to a digital control platform. The actuator is based on the class D amplifier and the sensor is implemented using a $\Sigma\Delta$ modulator to create a displacement-to-digital type sensor that is operated at 1 MHz.

I. Introduction

Nanopositioners are devices whose motion is controlled with nanometer precision [1]. Nanopositioners have found applications in areas such as microscopy, data storage, microfabrication and optics [1], [2], [3]. The use of microelectromechanical system (MEMS) technology to fabricate nanopositioner designs has become of interest to attain improved performance [3], [4], [5]. Miniaturizing the nanopositioner with MEMS technology aims to produce more complex devices with improved dynamics at minimum cost.

Transduction in MEMS can utilize a number of phenomena including piezoresistive, thermal , electrostatic, piezoelectric, and electromagnetic phenomena [3], [6], [7]. Electrostatic actuation is arguably the most common actuation method in MEMS due to its compatibility with any conductive material and low power consumption. Numerous MEMS nanopositioners utilize electrostatic actuation [3], [4], [5], [6], [8]. A key disadvantage of electrostatic actuation is its low force output for the same die area and applied voltage. In designs using electrostatic/capacitive sensing [7] or no sensing at all [4], [5], the transduction efficiency can be improved by utilizing the same drive simultaneously for actuation and sensing. Called self-sensing actuation, this simplifies the mechanical design and increases the effective die space that can be dedicated to a single drive.

Self-sensing electrostatic drives are implemented by time division multiplexing, whereby the drive is switched between actuation and sensing functions [9], [10], or spectral separation, whereby the actuation and sensing signals are separated by frequency [11]. An advantage of time division multiplexing is its suitability to be implemented with switching electronics. However, most implementations of this technique fully discharge the drive during the sensing phase. This reduces the maximum voltage that can be applied, thus reducing the range and maximum control effort available in a nanopositioning application [9], [10]. Secondly, fast switching electronics are typically restricted to low voltages. Thirdly microfabrication processes such as silicon-on-insulator produce devices where all drives share a common ground and are thus incompatible with a number of self-sensing techniques which requires each drive electrically isolated from one another [9], [10], [11], [12].

This article outlines a design of a switched self-sensing method for a MEMS electrostatic drive. It is applied to the MEMS nanopositioner reported by Maroufi *et al.* [13] which contains four electrostatic drives that actuate in the positive and negative directions along orthogonal axes. The method reported here overcomes the three limitations of similar self-sensing designs detailed in the introduction. Firstly, it allows the full supply voltage to be applied to the electrostatic drive at the sacrifice of actuator bandwidth. Secondly, it accommodates higher actuation voltages to drive the nanopositioner. Third, it is a one-terminal method which allows it to be applied to a set of drives with a common ground terminal.

Section II outlines the design of the electronics and FPGA components that comprise the actuation and sensing systems of the nanopositioner. Section III provides the open-loop identification of the nanopositioner to evaluate the performance of the developed self-sensing actuation method. Section IV explores an observed nonlinearity in the system due to imperfect isolation between the actuation and sensing systems.

II. Self-Sensing Actuator Operation

The MEMS nanopositioner upon which the proposed self-sensing actuation technique is applied to is shown in Figure 1. Each axis is driven by two opposing comb drives [7] which pull the central stage in the positive and negative directions. The stage is a common ground for both comb drives.

The sensor and actuator are implemented with switching electronics and are controlled from an FPGA. As both systems use the same comb drives, time division multiplexing is used to perform self-sensing. To perform the requisite switching, three phase signals are generated within the FPGA. The reset phase signal ϕ_1 is high when the sensor is zeroed before taking a measurement. The sensing phase signal ϕ_2 is high when the sensor is connected to the electrostatic drive. The actuating phase signal ϕ_a is high when the actuator is connected to the
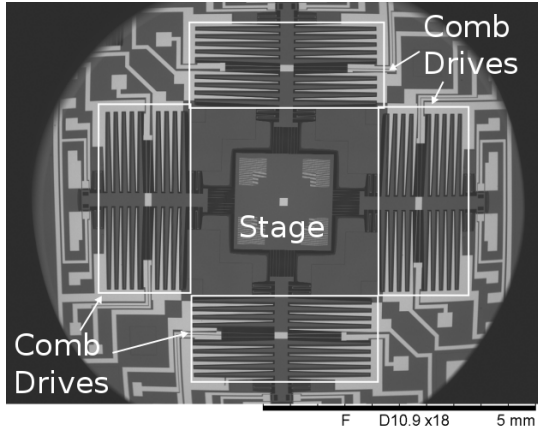
Fig. 1. The MEMS nanopositioner upon which the self-sensing actuation technique is applied to.

electrostatic drive. With the FPGA logic clocked at 200 MHz, the reset phase ϕ_1 is on for 130 cycles followed by a 10 cycle dead-time and the sensing phase ϕ_2 is on for 50 cycles followed by a 10 cycle dead-time. The actuating phase begins 10 cycles after the start of the reset phase and is high for 50 cycles.

The following subsections describe the theory and operation behind the sensor and actuator circuits. The sensor circuit is described first as its principle of operation influences the architecture of the actuator circuit.

A. Sensor

Comb drives consist of two electrodes with a comb shaped structure that employ electrostatic attraction to generate forces. In addition, the two electrodes form a capacitive structure whose capacitance is a function of displacement x. The capacitance C of a comb drive is [7]

$$C = \frac{n\varepsilon h}{g}(x + x_0) \qquad (1)$$

where n is the number of comb fingers, ε is the dielectric permittivity, h is the electrode height, g is the gap between fingers and x_0 is the initial electrode overlap. Each axis of the nanopositioner has two comb drives C_1 and C_2. Given the differential arrangement of the two comb drives, the capacitance of one drive increases with displacement while the other decreases, that is

$$C_1 = C_0 + \tfrac{1}{2}C_\Delta, \qquad (2)$$
$$C_2 = C_0 - \tfrac{1}{2}C_\Delta. \qquad (3)$$

The sensor measures C_Δ to eliminate the effect of the common mode capacitance and to increase the transduction efficiency. The capacitance C_Δ is

$$C_\Delta = C_1 - C_2 = \frac{2n\varepsilon h}{g}x = \beta x, \qquad (4)$$

where β is the constant of proportionality.

A charge balance type capacitive sensor [9], [14], [15], [16], shown in Figure 2, measures C_Δ. Prior to executing

a sensing phase, the actuator's output changes to a high impedance state to prevent interference with the sensing signal. As $C_1, C_2 \ll C_d$, the series combination of the comb drive and decoupling capacitor is dominated by the comb drive. From the perspective of the sensing circuit, both drives are charged to the positive rail $V_r = 3.3\,\text{V}$. When the sensing phase is executed the two drives are switched onto a charge amp in the C-to-V converter and the current that flows from the change in voltage is accumulated on the capacitances C_a. The gain of the C-to-V converter is

$$V_s = \frac{V_i - V_r}{C_a}C_\Delta + \frac{C_z}{C_a}V_z \qquad (5)$$

where V_i is the voltage at the input of the charge amp during the sensing phase and $C_a = 3.3\,\text{pF}$ is the charge amp capacitance. $C_z = 47\,\text{pF}$ and V_z are part of the zeroing circuit used to compensate for offsets that result from capacitance differences in both drives at zero displacement. The input voltage V_i during the sensing phase is constant and given as

$$V_i = \frac{V_{ocm}C_a + V_rC_0 + (V_{ocm} - V_{zcm})C_z}{C_a + C_0 + C_z}. \qquad (6)$$

Here $V_{ocm} = 1.65\,\text{V}$ and $V_{zcm} = 1.65\,\text{V}$. To maximize the gain of the C-to-V converter, V_i should be made as small as possible.

The voltage V_z is controlled via the zeroing signal z which is a unit-less value in the range $[-1, 1]$. A $\Sigma\Delta$ DAC maps the zeroing signal to the zeroing voltage with $V_z = V_r z$. The reconstruction filter in the zeroing circuit has a gain of 1 and a bandwidth of 0.482 Hz to suppress the quantization noise of the DAC and only pass constant signals.

The $\Sigma\Delta$ modulator [10], [17], [18], [19], [20] at the output of the sensor takes the output of the C-to-V converter and quantizes it. The output signal y is interpreted as 1 when high and −1 when low. The transfer function of the $\Sigma\Delta$ modulator is

$$\frac{y}{V_s} = \frac{1}{V_r}\frac{f_sC_s}{sC_i + f_sC_s}. \qquad (7)$$

With the integrating capacitor $C_i = 100\,\text{pF}$, the switching frequency $f_s = 1\,\text{MHz}$ and the sampling capacitor $C_s = 10\,\text{pF}$, the $\Sigma\Delta$ modulator has a gain 0.303 and a bandwidth of 15 915 Hz. Combining the characteristics of all the components of the sensor, the transfer function of the sensor from displacement x to the sensor output y is

$$H_s(s) = \frac{y}{x} = \frac{\beta f_s C_s(V_i - V_r)}{V_r C_a(sC_i + f_sC_s)}. \qquad (8)$$

B. Actuator

The actuators for the nanopositioner are shown in Figure 2. A $\Sigma\Delta$ modulator is used to generate the switching signals for the amplifier. The output is gated by the actuation phase signal ϕ_a, which while low, puts the amplifier into a high impedance state to prevent interference during the sensing phase. A half-bridge circuit is used to amplify the digital signal and the output is filtered by an RC filter whose capacitance is dominated by the sensor decoupling capacitor C_d.
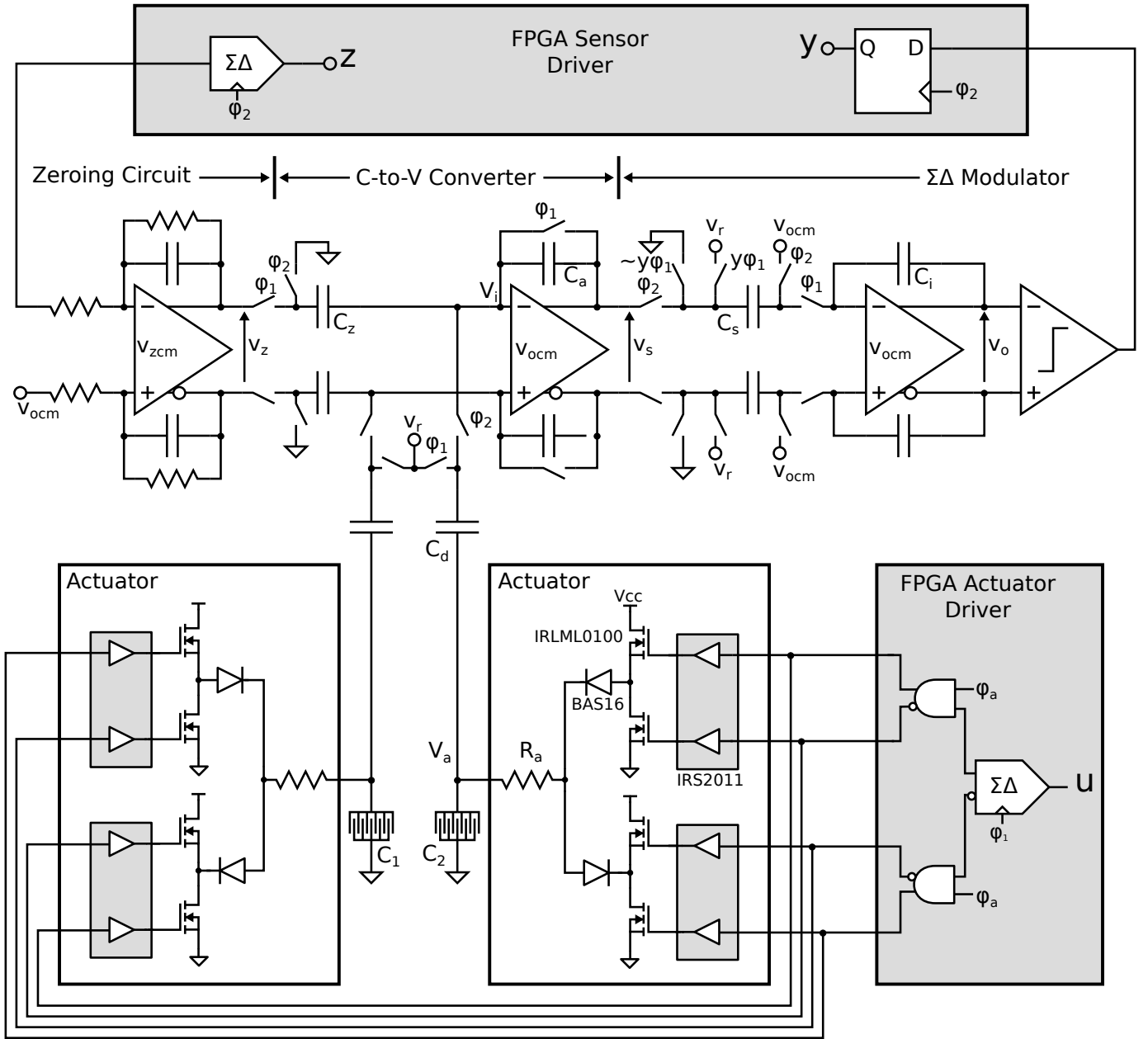
Fig. 2. A charge balance type capacitance sensor is utilized to measure the displacement of the nanopositioner. This converts the capacitance of the electrostatic drives to a voltage. The output of the C-to-V converter is fed into a $\Sigma\Delta$ circuit to digitize the signal. A zeroing circuit injects a charge into the C-to-V converter to compensate for any difference in capacitance between the two drives at zero displacement. For actuation, the FGPA controller uses $\Sigma\Delta$ modulation to perform digital to analog conversion and two half-bridges to amplify the signal. An RC filter suppresses quantization noise. The switch IC is the TS5A4596, the op-amp is the THS4121 and the comparator is the LMV7219, all from Texas Instruments. The MOSFETs and their drivers are from International Rectifier.

One half-bridge charges the comb drive and the other discharges. This arrangement provides the mechanism for forcing the amplifier into a high impedance state at high sampling rates. At the output of each half-bridge is a diode whose orientation in Figure 2 indicates whether the amplifier is used for charging or discharging. In the case of the charging amplifier, the high side MOSFET is switched on to charge the electrostatic drive. When going into a high impedance state, simply switching off the MOSFET is too slow, there are parasitic capacitances within the MOSFET that need to be

discharged. Switching on the low side MOSFET turns off the high side MOSFET and the diode moving the amplifier into a high output impedance state.

The control action u is a unit-less number in the range $[-1, 1]$ and the ideal amplifier maps the input to an actuator voltage V_a in the range $[0, V_{cc}]$. For the RC filter, opening the half-bridge every cycle in effect creates a switched resistor RC filter. Let D_a be the duty cycle for which the actuation is connected to the RC filter with resistance R_a and thus the equivalent resistance of the switched resistor is R_a/D_a. The
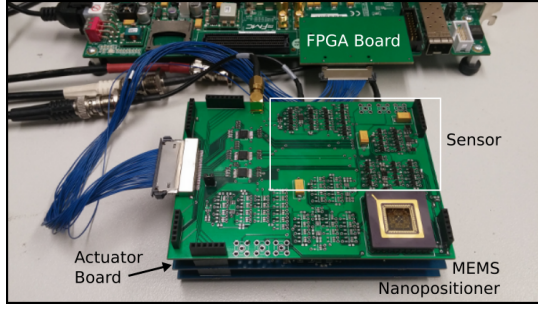
Fig. 3. The fabricated nanopositioner system. The MEMS nanopositioner is seen in the lower right corner of the circuit board. Adjacent to the MEMS device is the sensing circuitry. The boards stacked under the sensor comprise of the actuator circuits and the power supply. The system is connected to a development board housing the Xilinx Kintex 7 FPGA which controls the system.
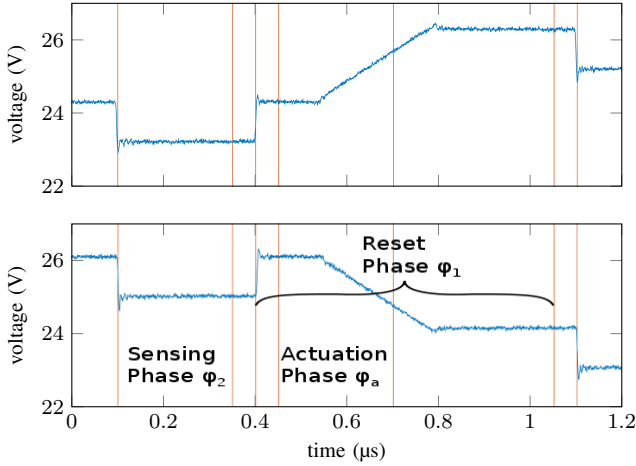

Fig. 4. The voltage waveforms at opposing electrostatic drives over 1.2 sampling periods.

transfer function of the actuator is

$$H_a(s) = \frac{V_a}{u} = \frac{V_{cc}}{2} \frac{D_a}{R_a C_d s + D_a}.$$ (9)

In the implemented system, $V_{cc} = 50\,\mathrm{V}$, $R_a = 3.3\,\mathrm{k\Omega}$, $C_d = 820\,\mathrm{pF}$ and $D_a = 0.25$. The gain of the system is 25 and the bandwidth is $14\,527\,\mathrm{Hz}$.

A photo of the fabricated system is shown in Figure 3.

III. Open Loop Characterization

To show the correct operation of the time-multiplexed switching scheme, Figure 4 shows the actuator voltage on the opposing electrostatic drives with $u = 0$. The switching cycle begins with the sensing phase which can be seen by a step of approximately 1 V in both waveforms for a duration of 250 ns. After a 50 ns wait, the ϕ_1 phase resets the capacitance-to-voltage converter and the voltages return to their previous values. After a further 50 ns the actuation phase begins and the amplifier is turned on. To protect the bridge circuits in the amplifier, a shoot through delay of 50 ns causes the delay in the amplifier response. The actuation phase lasts for 250 ns after which there is a 350 ns wait to allow the actuator time to
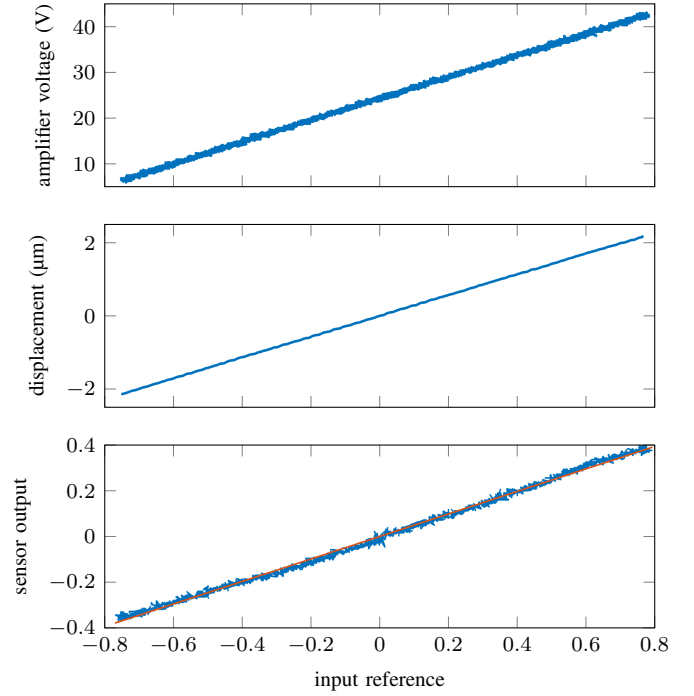

Fig. 5. The large signal responses of the system. The nanopositioner displacement is measured with a laser vibrometer. The sensor output is filtered with a fourth order 10 kHz low pass Butterworth filter to remove the quantization noise.

open-circuit. Once the amplifier is open circuit, ϕ_1 is set low and after 50 ns the sensing phase is executed again.

To determine the sensitivies of the various components of the system, the control action u is set to a 0.5 Hz triangle wave which ramps between ± 0.75 while the actuator voltage V_a, nanopositioner displacement x and sensor output y are measured. These results are shown in Figure 5. The amplifier is linear and has a gain of 23.53 V. The mapping from system input to displacement is linear and has a gain of 2.828 µm. The differential arrangement has eliminated the quadratic nonlinearity of comb drives [7]. The mapping from control action to sensor output has a gain of 0.4931. A slight nonlinearity is observed in this response. With these gains, the sensitivity of the sensor is $0.1744\,\mathrm{µm^{-1}}$.

Figure 6 shows the frequency response of the nanopositioner from the control action u to the sensor output y using stepped-sine measurements. Using complex curve fitting, a fourth order linear model was found to fit to the measured response. Its transfer function is

$$G(s) = \frac{-0.078541(s+1.463 \times 10^6)(s-8589)(s^2+5929s+5.773 \times 10^8)}{(s+1.107 \times 10^5)(s+1.241 \times 10^4)(s^2+339.8s+6.742 \times 10^8)}.$$ (10)

The frequency of the complex poles at 4.133 kHz matches the mechanical dynamics of the nanopositioner. The higher frequency real pole at 17.62 kHz is associated with the bandwidth of the actuator and sensor. However, the dynamics associated with the pole at 1975 Hz are unexpected but can be clearly seen in the phase role off. This dynamic is attributed to the feedthrough from the actuator to sensor. This feedthrough
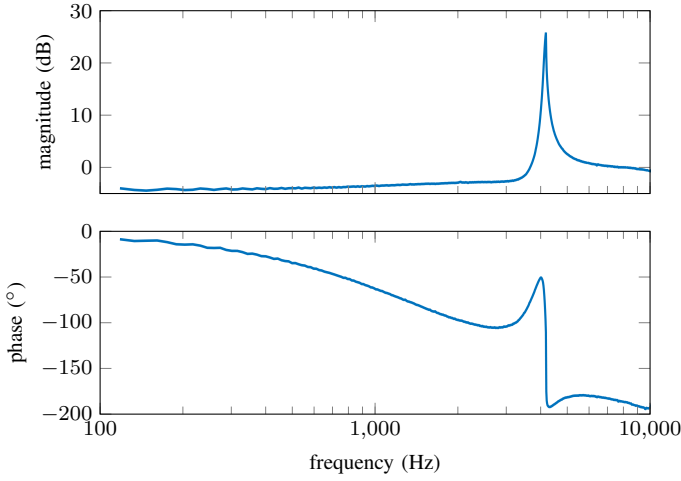
Fig. 6. The frequency response of the nanopositioner from the control action to the sensor output. A fourth order model fits well to the frequency response and this models is used for control design.

(a) Harmonic response at 122 Hz
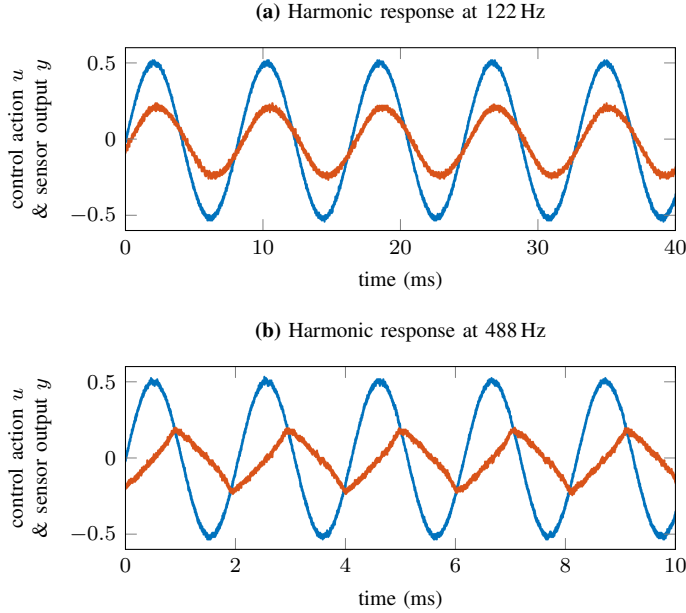
(b) Harmonic response at 488 Hz

Fig. 7. Nonlinear distortion of the harmonic response of the nanopositioner. In both measurements the control action u (the larger signal in both plots) is set to a sine wave of amplitude 0.5. **(a)** The harmonic response of the nanopositioner at 122 Hz. **(b)** The harmonic response at 488 Hz.

causes nonlinear dynamics in the nanopositioning system and is discussed in the next section.

IV. NONLINEAR DYNAMICS

The nonlinearity observed in Figure 5 and the additional dynamics observed in Figure 6 are associated with the fact that the sensor picks up any current flowing into it and perfect isolation is impossible. Currents present include the displacement measurement, the motional current of the nanopositioner, reverse bias currents through the diodes, leakage currents in the switches and currents due to parasitic capacitances in the switches.
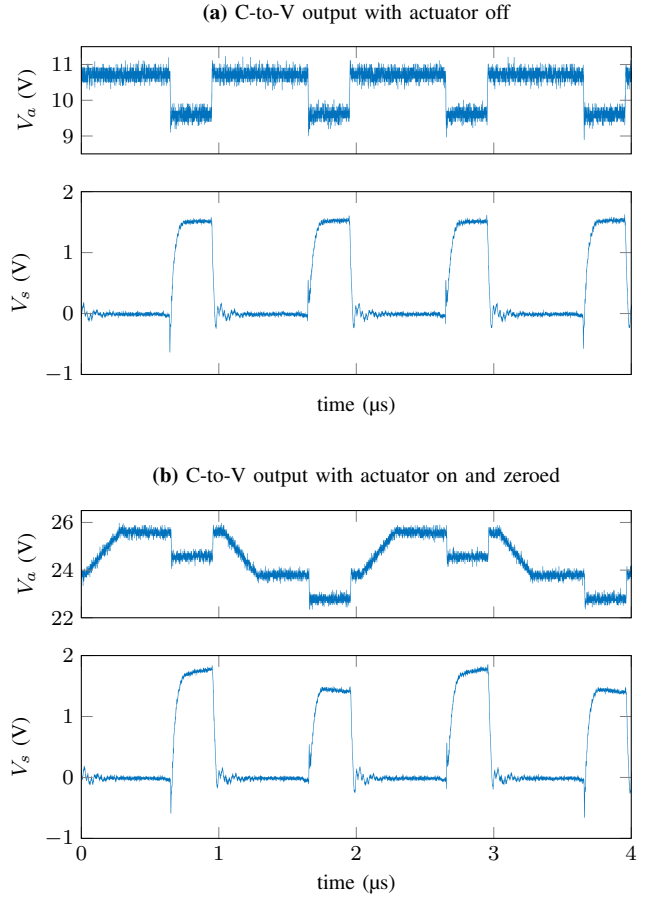

(a) C-to-V output with actuator off

(b) C-to-V output with actuator on and zeroed

Fig. 8. The capacitive measurement at the output of the C-to-V converter V_s without **(a)** and with **(b)** the actuator. It is shown with the actuator voltage V_a.

The first observation is that the distortion in the sensor signal is frequency dependent. With the control action u set to sine wave of amplitude 0.5, Figure 7 shows the sensor output y at 122 Hz and 488 Hz. At the lower frequency, the distortion appears relatively small, while at the higher frequency, the distortion appears relatively large. When the nanopositioner starts to resonate, linearity appears to return to the sensor output as the displacement measurement becomes relatively large.

Investigation into the cause of the nonlinear dynamics revealed an issue with the isolation between the actuator and sensing circuits. Figure 8 shows the output voltage of C-to-V converter V_s for two cases: one with actuator off and the other with the actuator on and the control action u set to zero. With the actuator off, each measurement sample is consistently of the same value. With the actuator on, an offset appears in each measurement sample. The polarity of this offset correlates with whether the electrostatic drive was charged or discharged during the previous actuating phase. This reveals that current is leaking from the actuator into the sensor during the sensing phase. Furthermore, the nonlinear dynamics are related to the quantized version of the control action u that is used to control the amplifiers.

V. Conclusion

The design provides a switching electronics based method to control the displacement of an electrostatic MEMS device. It is theoretically linear, can handle high voltages, is compatible with the silicon-on-insulator microfabrication process and is directly controllable from a digital platform.

However, the most significant issue evident with the design is the dynamics associated with the leakage of current from the actuator into the sensor during the sensing phase. The presence of these dynamics reduces the precision of the nanopositioning system. The magnitude of the current leaking into the sensor would be quite small but of a similar order of magnitude to the current associated with the displacement measurement. The immediate conclusion is that the proposed actuator architecture is inappropriate in the current instrumentation context.

References

[1] N. B. Hubbard, M. L. Culpepper, and L. L. Howell, "Actuators for micropositioners and nanopositioners," *Applied Mechanics Reviews*, vol. 59, pp. 324–334, Nov. 2006.

[2] B. Sahu, K. K. Leang, and C. R. Taylor, "Emerging challenges of microactuators for nanoscale positioning, assembly, and manipulation," *Journal of Manufacturing Science and Engineering*, vol. 132, p. 030 917, 2010.

[3] M. Maroufi, A. Bazaei, and S. O. R. Moheimani, "A high bandwidth MEMS nanopositioner for on-chip AFM: Design, characterization and control," *IEEE Transactions on Control Systems Technology*, 2015, Accepted for publication, published.

[4] X. Liu, K. Kim, and Y. Sun, "A MEMS stage for 3-axis nanopositioning," *Journal of Micromechanics and Microengineering*, vol. 17, no. 9, p. 1796, 2007.

[5] A. G. Fowler, A. N. Laskovski, A. C. Hammond, and S. O. R. Moheimani, "A 2-DoF electrostatically actuated MEMS nanopositioner for on-chip AFM," *IEEE/ASME Journal of Microelectromechanical Systems*, vol. 21, no. 4, pp. 771–773, 2012.

[6] L. Sun, J. Wang, W. Rong, X. Li, and H. Bao, "A silicon integrated micro nano-positioning xy -stage for nano-manipulation," *Journal of Micromechanics and Microengineering*, vol. 18, no. 12, p. 125 004, 2008.

[7] V. Kaajakari, *Practical MEMS*. Small Gear Publishing, 2009.

[8] B. Koo, X. Zhang, J. Dong, S. Salapaka, and P. Ferreira, "A 2 degree-of-freedom SOI-MEMS translation stage with closed-loop positioning," *Microelectromechanical Systems, Journal of*, vol. 21, no. 1, pp. 13–22, Feb. 2012.

[9] Y. Liang, L. Xiaowei, C. Weiping, and Z. Zhiping, "High resolution interface circuit for closed-loop accelerometer," *Journal of Semiconductors*, vol. 32, no. 4, p. 045 005, 2011.

[10] P. Lajevardi, V. Petkov, and B. Murmann, "A $\Delta\Sigma$ interface for MEMS accelerometers using electrostatic spring constant modulation for cancellation of bondwire capacitance drift," *Solid-State Circuits, IEEE Journal of*, vol. 48, no. 1, pp. 265–275, Jan. 2013.

[11] J. Dong and P. M. Ferreira, "Simultaneous actuation and displacement sensing for electrostatic drives," *Journal of Micromechanics and Microengineering*, vol. 18, no. 3, p. 035 011, 2008.

[12] L. Aaltonen and K. Halonen, "Continuous-time interface for a micromachined capacitive accelerometer with NEA of $4\mu g$ and bandwidth of 300Hz," *Sensors and Actuators A: Physical*, vol. 154, no. 1, pp. 46 –56, 2009.

[13] M. Maroufi and S. Moheimani, "A 2DOF SOI-MEMS nanopositioner with tilted flexure bulk piezoresistive displacement sensors," *Sensors Journal, IEEE*, vol. PP, no. 99, pp. 1–1, 2015.

[14] W. Bracke, P. Merken, R. Puers, and C. V. Hoof, "Ultra-low-power interface chip for autonomous capacitive sensor systems," *IEEE Transactions on Circuits and Systems I: Regular Papers*, vol. 54, no. 1, pp. 130–140, Jan. 2007.

[15] S. Xia and S. Nihtianov, "Power-efficient high-speed and high-resolution capacitive-sensor interface for sub-nanometer displacement measurements," *Instrumentation and Measurement, IEEE Transactions on*, vol. 61, no. 5, pp. 1315–1322, May 2012.

[16] H. Song, Y. Park, H. Kim, D.-i. D. Cho, and H. Ko, "Fully integrated low-noise readout circuit with automatic offset cancellation loop for capacitive microsensors," *Sensors*, vol. 15, no. 10, p. 26 009, 2015.

[17] R. Schreier and G. Temes, *Understanding delta-sigma data converters*. Wiley-IEEE Press, 2005.

[18] J. O'Dowd, A. Callanan, G. Banarie, and E. Company-Bosch, "Capacitive sensor interfacing using sigma-delta techniques," in *Sensors, 2005 IEEE*, Oct. 2005, 4 pp.–.

[19] D.-Y. Shin, H. Lee, and S. Kim, "A delta–sigma interface circuit for capacitive sensors with an automatically calibrated zero point," *Circuits and Systems II: Express Briefs, IEEE Transactions on*, vol. 58, no. 2, pp. 90–94, Feb. 2011.

[20] Y. Jung, Q. Duan, and J. Roh, "A 17.4-bit delta-sigma capacitance-to-digital converter for one-terminal capacitive sensors," *IEEE Transactions on Circuits and Systems II: Express Briefs*, vol. PP, no. 99, pp. 1–1, 2015.